JGR Space Physics

RESEARCH ARTICLE
10.1029/2020JA027796

Nondiffusive Pitch-Angle Scattering of a Distribution of Energetic Particles by Coherent Whistler Waves

Young Dae Yoon[1] and **Paul M. Bellan**[1]

[1]Department of Applied Physics and Materials Science, California Institute of Technology, Pasadena, CA, USA

Key Points:
- A much improved condition is provided for how coherent whistler waves scatter the pitch-angle of energetic particles
- A significant fraction of energetic, thermally distributed particles undergoes this scattering
- The theory reveals a critical mechanism not contained in the widely used second-order trapping theory

Correspondence to:
Y. D. Yoon,
yyoon@caltech.edu

Citation:
Yoon, Y. D., & Bellan, P. M. (2020). Nondiffusive pitch-angle scattering of a distribution of energetic particles by coherent whistler waves. *Journal of Geophysical Research: Space Physics*, *125*, e2020JA027796. https://doi.org/10.1029/2020JA027796

Received 10 JAN 2020
Accepted 5 MAY 2020
Accepted article online 11 JUN 2020

Abstract Whether or not coherent magnetospheric whistler waves play important roles in the pitch-angle scattering of energetic particles is a crucial question in magnetospheric physics. The interaction of a thermal distribution of energetic particles with coherent whistler waves is thus investigated. The distribution is prescribed by the Maxwell-Jüttner distribution, which is a relativistic generalization of the Maxwell-Boltzmann distribution. Coherent whistler waves are modeled by circularly polarized waves propagating parallel to the background magnetic field. It is shown that for parameters relevant to magnetospheric chorus, a significant fraction (1–5%) of the energetic particle population undergoes drastic, nondiffusive pitch-angle scattering by coherent chorus. The scaling of this fraction with the wave amplitude may also explain the association of relativistic microbursts to large-amplitude chorus. A much improved condition for large pitch-angle scattering is presented that is related to, but may or may not include the exact resonance condition depending on the particle's initial conditions. The theory reveals a critical mechanism not contained in the widely used second-order trapping theory.

Plain Language Summary A certain class of plasma waves called whistler waves is abundant in the Earth's magnetosphere. The interaction between whistler waves and energetic particles trapped in the Earth's magnetic field can cause the particles to escape the trap and cause pulsating auroras or damage spacecraft. Although previous studies have mostly focused on diffusive mechanisms, we show that a significant fraction of the energetic particles interacts nondiffusively or coherently with the wave. We also show that a widely used condition for such interaction is incomplete and provide a more accurate alternative.

1. Introduction

Whistler waves are right-handed circularly polarized electromagnetic plasma waves that are ubiquitous in the Earth's magnetosphere (Burtis & Helliwell, 1969; Gurnett & O'Brien, 1964; Russell et al., 1969; Tsurutani & Smith, 1974), Jupiter's magnetosphere (Leubner, 1982; Sentman & Goertz, 1978; Tsurutani et al., 1993), and Saturn's magnetosphere (Akalin et al., 2006; Barbosa & Kurth, 1993; Hospodarsky et al., 2008). These waves are also important in the solar wind (Coroniti et al., 1982; Vocks et al., 2005), fast magnetic reconnection (Bellan, 2014; Chai et al., 2016; Haw et al., 2019; Mandt et al., 1994; Yoon & Bellan, 2017, 2018), and helicon plasma sources (Boswell, 1984; Chen & Boswell, 1997). In particular, the interaction between energetic charged particles and magnetospheric whistler waves is important since the interaction can change the pitch-angle of the particles, potentially scattering them into the loss cone of a magnetic mirror configuration such as the Earth's dipole magnetic field. Because the escaped energetic particles can cause pulsating auroras at the Earth's poles, and energetic particles in general can damage spacecraft, this interaction has been the focus of many studies for decades (Albert, 2005; Artemyev et al., 2013, 2016; Helliwell & Crystal, 1973; Horne & Thorne, 2003; Kennel & Petschek, 1966; Lyons et al., 1971; Lyons, 1974; Omura & Summers, 2006; Summers et al., 1998; Tsurutani et al., 2013).

Relativistic wave-particle resonance has been known to be an important element of particle energization and pitch-angle scattering. Resonant interaction arises when

$$\omega - kv_z = \frac{\Omega}{\gamma}. \tag{1}$$

Here, ω is the wave frequency, k is the wavenumber parallel to the background magnetic field B_0, which is oriented in the z direction, v_z is the parallel particle velocity, and $\Omega = qB_0/m$ is the cyclotron frequency

of the particle with charge q and mass m. Also, $\gamma = \left(1 - v^2/c^2\right)^{-1/2}$ is the particle Lorentz factor where v is the particle speed and c is the speed of light. Kennel and Petschek (1966) first quantified the scattering mechanism by which incoherent whistler waves lead to velocity space diffusion, and numerous studies have further developed this mechanism (Albert, 2005; Lyons et al., 1971; Lyons, 1974; Tsurutani et al., 2009). However, recent spacecraft measurements indicate that the observed chorus bursts are, in fact, extremely coherent and that these waves, especially large-amplitude ones ($\delta B/B_0 \sim 0.01$ where δB is the wave magnetic field), are directly linked to electron energization, loss, and microbursts (Anderson & Milton, 1964; Breneman et al., 2017; Cattell et al., 2008; Gao et al., 2014; Tsurutani et al., 2009, 2013). This linkage suggests that a nondiffusive process could be governing what is observed.

There has thus been a continuing and substantial theoretical effort to investigate the dynamics of energetic particles under coherent whistler waves. Bortnik et al. (2008) numerically investigated ad hoc the coherent interaction between large-amplitude whistler waves and relativistic particles. Lakhina et al. (2010) showed via calculations of pitch-angle diffusion coefficients that coherent chorus subelements can cause rapid pitch angle scattering, although Lakhina et al. (2010) used diffusion coefficients calculated from incoherent whistler waves (Kennel & Petschek, 1966) and used nonrelativistic equations of motion whereas the actual wave-particle interaction involves relativistic particles (10 keV to MeV Breneman et al., 2017; Tsurutani et al., 2013). Bellan (2013) presented an exact analytical calculation involving a relativistic particle in a right-handed circularly polarized electromagnetic wave. This calculation showed that a certain class of particles undergo quick, drastic pitch-angle scattering depending on whether the individual particle's initial conditions meet a certain criterion, which will be discussed in the next section. Also note that other studies have investigated this single-particle problem via various methods (Bourdier & Gond, 2000; Ginet & Heinemann, 1990; Qian, 2000; Roberts & Buchsbaum, 1964). However, an analysis of the importance of this mechanism for a distribution of particles has not yet been done. To demonstrate importance, one must show that a significant fraction of the particles in the distribution experiences this drastic scattering. If this can be demonstrated, then the particle interaction with coherent whistler waves will be a dominant pitch-angle scattering mechanism.

We extend in this paper the analysis presented in Bellan (2013) to the relativistic generalization of a thermal distribution of particles; the generalization is prescribed by the Maxwell-Jüttner distribution (Jüttner, 1911). It is found that for parameters relevant to magnetospheric chorus, coherent right-handed circularly polarized waves propagating parallel to the background magnetic field trigger large, nondiffusive pitch-angle scatterings for a significant fraction (1%–5%) of the energetic particles. The scaling of this fraction with the wave amplitude may also explain the association of relativistic microbursts to large-amplitude chorus (Breneman et al., 2017). A new condition for large pitch-angle scattering is also presented; this condition specifies a certain range related to Equation 1, but may or may not include exact resonance depending on the particle initial conditions. Test-particle simulations corroborate the predictions made by this analysis. It is also demonstrated that the widely used second-order trapping theory (Omura et al., 1991, 2007, 2008; Nunn, 1974; Sudan & Ott, 1971) is a simplified approximation of the theory presented in this paper and that this simplified approximation effectively misses critical details of the wave-particle interaction. The present study illustrates that coherent whistler waves are an important cause of nondiffusive pitch-angle scattering and provides an accurate condition for this scattering.

2. Two-Valley Motion Review

Let us begin with a brief review of the large pitch-angle scattering mechanism presented in Bellan (2013). A thorough comprehension of this single-particle mechanism is essential for understanding the ensuing analysis presented here. It is assumed that the wave is right-handed circularly polarized and travels parallel to a uniform background magnetic field, so the total magnetic field can be expressed as $\mathbf{B} = B_0\hat{z} + \tilde{\mathbf{B}}$ where

$$\tilde{\mathbf{B}} = \kappa B_0 \left[\hat{x}\sin(kz - \omega t) + \hat{y}\cos(kz - \omega t)\right]. \tag{2}$$

Here, κ is the wave amplitude relative to the background B_0. Faraday's law determines the wave electric field to be

$$\tilde{\mathbf{E}} = -\frac{\omega}{k}\hat{z} \times \tilde{\mathbf{B}} = \frac{\omega}{k}\tilde{B}\left[\hat{x}\cos(kz - \omega t) - \hat{y}\sin(kz - \omega t)\right]. \tag{3}$$

The relativistic Lorentz force equation determines the motion of a charged particle:

$$\frac{d}{dt}(\gamma\boldsymbol{\beta}) = \frac{q}{m}\left(\frac{\tilde{\mathbf{E}}}{c} + \boldsymbol{\beta}\times\mathbf{B}\right), \tag{4}$$

where $\beta = \mathbf{v}/c$ and $\gamma = \left(1-\beta^2\right)^{-1/2}$.

In Bellan (2013), a left-handed circularly polarized wave was used although the study was intended for right-handed waves. However, the result therein is unaffected by this apparent error because the sign of the particle charge was unspecified. Although it was not explicitly stated, the analysis was carried out assuming that the charge is positive, for example, for positrons or ions. If the charge is assumed to be negative, the same wave-particle interaction arises when the wave is assumed to have a right-handed polarization. Therefore, the theory in Bellan (2013) describes wave-particle interactions between positively charged particles and left-handed waves, and equivalently between negatively charged particles and right-handed waves—or electrons and right-handed whistler waves. This equivalence can also be seen using charge-parity-time symmetry, which is a fundamental law of any Lorentz-invariant system (Greenberg, 2002); making the changes $z \to -z$ and $t \to -t$ in Equations 2 and 3 changes the sense of rotation of the wave, and the relevant physics must be equivalent when the change $q \to -q$ is made.

In this paper, the analysis in Bellan (2013) with the left-handed wave and positively charged particles will be used for two reasons. First, the analysis can then be kept general for any particle with any sign of charge. Second, the derivation of a separate theory for negatively charged particles will merely be a matter of some sign changes and is not worth the additional complexity in understanding the core points of this paper.

In Bellan (2013), a "frequency mismatch" parameter

$$\xi = 1 + \alpha\gamma\left(n\beta_z - 1\right) \tag{5}$$

was defined, where $\alpha = \omega/\Omega$ is the normalized frequency, $\beta_z = v_z/c$ is the normalized parallel velocity, and $n = ck/\omega$ is the refractive index. Equation 1 is satisfied when $\xi = 0$, so ξ is a measure of the departure from resonance. An exact rearrangement of Equation 4 leads to an equation of motion for a particle moving in ξ-space (Bellan, 2013):

$$\frac{1}{\Omega'}\frac{d^2\xi}{dt'^2} = -\frac{\partial\psi}{\partial\xi}, \tag{6}$$

where

$$\psi(\xi) = \frac{1}{8}\xi^4 + \left(\kappa'^2 - \frac{\xi_0^2}{2} - s\kappa'\sin\phi_0\right)\frac{\xi^2}{2} - \kappa'^2\xi \tag{7}$$

is the pseudo-potential for ξ-space motion. Here, the primed quantities are calculated in the wave frame, that is, a frame moving with a velocity $\hat{z}\omega/k$. The subscript 0 refers to the value at the initial time $t = t' = 0$ and there are two parameters, namely, s and ϕ_0. The parameter s is defined as

$$s = \frac{\alpha n\beta_{\perp 0}\gamma_0}{\gamma_T} = \frac{k\rho_0}{\gamma_T}, \tag{8}$$

where $\gamma_T = \left(1-n^{-2}\right)^{-1/2}$ is the Lorentz factor of the wave, and ρ is the relativistic Larmor radius. The parameter ϕ_0 is defined as the initial angular orientation of the perpendicular velocity in the $x-y$ plane, that is, the angle between $\beta_{\perp 0}$ and $\tilde{E}(t=0, z=0)$. The shape of the pseudo-potential is entirely determined by the initial conditions of the particle with respect to the wave as prescribed by ξ_0, s, and ϕ_0. Note that s is an initial condition of the particle because α and n are fixed parameters in the present analysis.

Multiplying Equation 6 by $d\xi/dt'$ and integrating with respect to t' yields the particle pseudo-energy,

$$W = \frac{1}{2\Omega'^2}\left(\frac{d\xi}{dt'}\right)^2 + \psi(\xi), \tag{9}$$

which is a constant of the motion. For certain initial conditions, $\psi(\xi)$ consists of two valleys separated by a hill in between. If the initial particle pseudo-energy is sufficiently large to go over the hill between the two valleys, then the particle undergoes two-valley motion in ξ-space. This motion involves large changes in ξ and thus in β_z, $\beta_\perp$ and the pitch-angle $\theta_{\text{pitch}} = \tan^{-1}\beta_\perp/\beta_z$.

3. Two-Valley Motion Condition

Let us now derive the conditions for two-valley motion for a given particle. The conditions consist of two parts: $\psi(\xi)$ must first be two-valleyed, and the particle must have sufficient pseudo-energy to overcome the hill between the two-valleys. The initial particle kinetic pseudo-energy can be expressed as (Bellan, 2013)

$$\frac{1}{2\Omega'^2}\left(\frac{d\xi}{dt'}\right)^2_{t'=t=0} = \frac{1}{2}s^2\kappa'^2\cos^2\phi_0, \tag{10}$$

so the total pseudo-energy is

$$W = \frac{1}{2}s^2\kappa'^2\cos^2\phi_0 - \frac{\xi_0^4}{8} + \frac{\xi_0^2}{2}\kappa'\left(\kappa' - s\sin\phi_0\right) - \kappa'^2\xi_0. \tag{11}$$

We write Equation 7 as $\psi(\xi) = \xi^4/8 + b\xi^2/2 - \kappa'^2\xi$ where $b = \kappa'^2 - \xi_0^2/2 - s\kappa'\sin\phi_0$. Then $d\psi/d\xi = \xi^3/2 + b\xi - \kappa'^2$, so one extremum is at small $\xi \simeq \kappa'^2/b$ and two extrema are at large $\xi \simeq \pm\sqrt{-2b}$. Since $d^2\psi/d\xi^2 = 3\xi^2/2 + b$, for $b < 0$, the large extrema are local minima (two valleys) and the small extremum is a local maximum (a hill). For $b \geq 0$, the large extrema are undefined, so there is a minimum at $\xi \simeq \kappa'^2/b$. Figure 1a shows an example of a two-valley $\psi(\xi)$ for which $b < 0$, and Figure 1b shows a one-valley $\psi(\xi)$ for which $b \geq 0$.

We now make the assumption

$$\kappa' \ll s, \tag{12}$$

which will be shown in section 5 to be appropriate for relevant magnetospheric situations. Then, $b \simeq -\xi_0^2/2 - s\kappa'\sin\phi_0$ is negative for

$$\xi_0^2 \geq -2s\kappa'\sin\phi_0. \tag{13}$$

All particles having $\sin\phi_0 > 0$ satisfy this equation because ξ_0^2 is nonnegative. Particles having $\sin\phi_0 \leq 0$ satisfy Equation 13 only if they are a certain distance away from exact resonance ($\xi = 0$).

Now, inserting $\xi = \kappa'^2/b$ in Equation 7, we have the height of the hill to be $\psi_{max} \simeq -\kappa'^4/(2b)$. Therefore, the particle has enough pseudo-energy to cross over the hill if

$$\frac{1}{2}s^2\kappa'^2\cos^2\phi_0 - \frac{\xi_0^4}{8} + \frac{\xi_0^2}{2}\kappa'\left(\kappa' - s\sin\phi_0\right) \geq \kappa'^2\xi_0 - \frac{\kappa'^4}{2b}. \tag{14}$$

We now assume and justify later that the terms on the right-hand side of Equation 14 are much smaller than those on the left-hand side. Using Equation 12, Equation 14 becomes

$$\frac{1}{2}s^2\kappa'^2\cos^2\phi_0 - \frac{\xi_0^4}{8} - \frac{\xi_0^2}{2}\kappa' s\sin\phi_0 \geq 0, \tag{15}$$

whose solution is

$$\xi_0^2 \leq 2s\kappa'\left(1 - \sin\phi_0\right). \tag{16}$$

Now we derive the conditions for which the assumptions regarding Equation 14 are valid. This is done by using the solution (i.e., Equation 16) obtained under the assumptions and deriving the conditions for which the terms on the right-hand side of Equation 14 are indeed small compared to those on the left-hand side. Using Equation 16 as an equality, it is seen that each term on the left-hand side of Equation 14 is $O\left(s^2\kappa'^2\right)$ except for the $\kappa'^2\xi_0^2/2$ term, which is ignored by Equation 12. On the right-hand side, $\kappa'^2\xi_0 = O\left(\sqrt{s\kappa'^5}\right)$ so it can be ignored if $\kappa' \ll s^3$. Examining the second term, $\kappa'^4/2b = O\left(\kappa'^3/s\right)$ because $b = O\left(s\kappa'\right)$, so it can be ignored if $\kappa' \ll s$. Since $\kappa' \ll 1$ for linear waves, $\kappa' \ll s^3$ and $\kappa' \ll s$ are both true for $s \geq 1$, and $\kappa' \ll s^3$ is a stronger statement than $\kappa' \ll s$ if $s < 1$. Therefore, for $\kappa' \ll s^3$—which will later be demonstrated to be valid for relevant magnetospheric parameters—the following gives the condition for which a particle undergoes two-valley motion and thus a large pitch-angle scattering:

$$-2s\kappa'\sin\phi_0 \leq \xi_0^2 \leq 2s\kappa'\left(1 - \sin\phi_0\right). \tag{17}$$

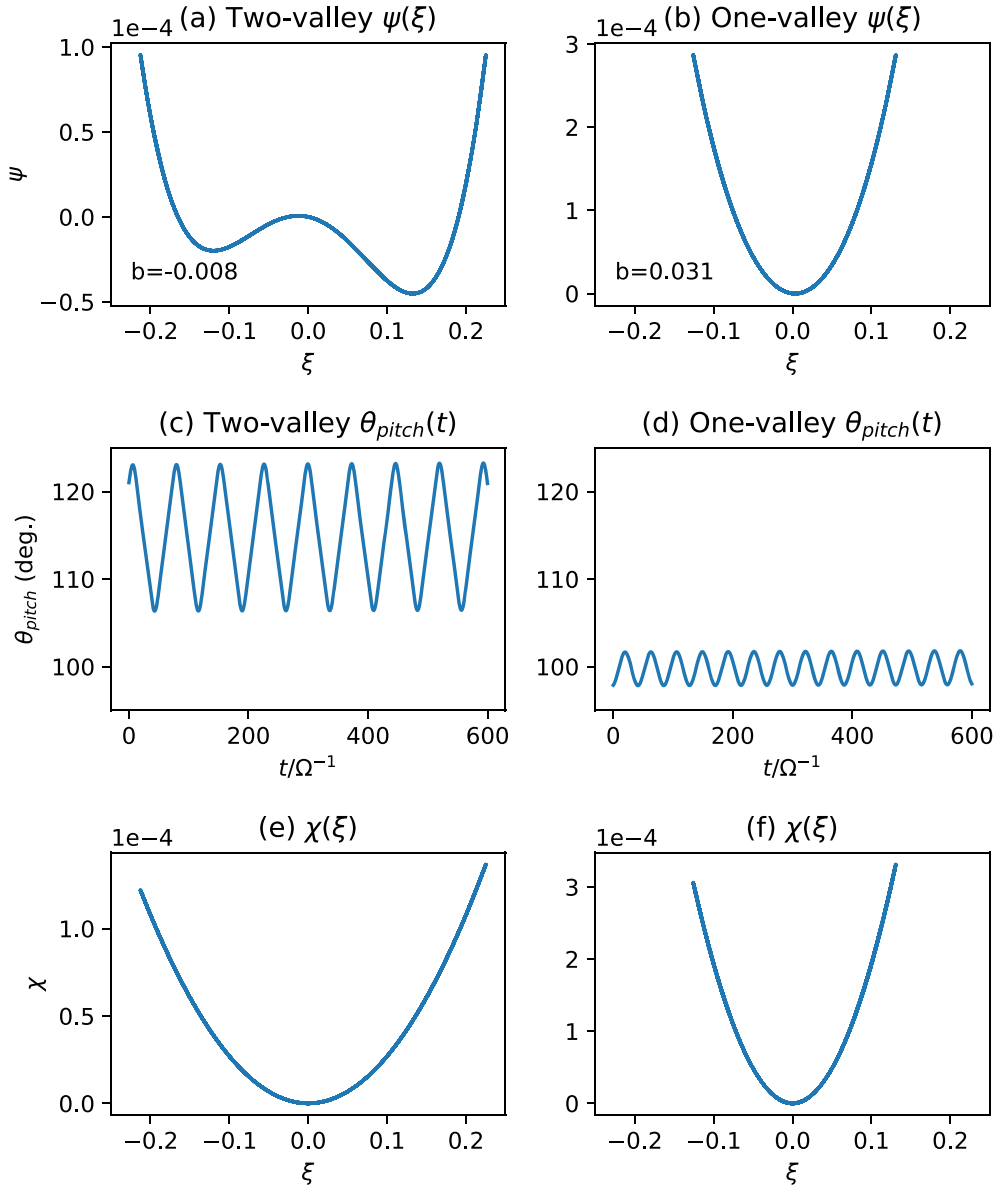

Figure 1. (a) An example of a two-valley $\psi(\xi)$ for which $b = -0.008 < 0$. (b) An example of a one-valley $\psi(\xi)$ for which $b = 0.031 \geq 0$. (c) The time-dependent pitch-angle of the particle undergoing two-valley motion, and (d) that of the particle undergoing one-valley motion. The wave parameters were $\kappa = 0.01$, $\alpha = 0.25$, and $n(\alpha) = 18$ from Equation 28. (e,f) The approximated pseudo-potentials χ obtained by keeping only the term involving $s\kappa'$ in Equation 7 for the respective particles.

Equation 17 is one of the main results of this paper. For $\phi_0 \geq 0$, Equation 17 becomes Equation 16 and specifies a certain range around $\xi_0 = 0$. However, for $\phi_0 < 0$ that statistically represents half of the particle population, Equation 17 does not include $\xi_0 = 0$, which means that particles further away from exact resonance undergo two-valley motion and thus large pitch-angle scattering. Therefore, Equation 17 specifies the exact range of the initial distance from resonance that leads to two-valley motion.

Figure 1c shows the time-dependent pitch-angle $\theta_{\text{pitch}}(t)$ of the particle that has enough pseudo-energy to undergo two-valley motion in the two-valley pseudo-potential in Figure 1a. Figure 1d shows $\theta_{\text{pitch}}(t)$ of the particle moving in the one-valley pseudo-potential. The particle in Figure 1c experiences a much larger change in pitch-angle than that in Figure 1d. The rate of change of the pitch-angle in Figure 1c is also very large; the wave period is $T_{\text{wave}}\Omega = 2\pi/\alpha \simeq 25$, so the pitch-angle changes by ~15° in $t\Omega \simeq 40$ or in about one to two wave periods.

4. Distribution of ξ

The initial particle distribution in ξ-space will now be derived. The subscript zero will henceforth be dropped because only the initial conditions are being examined. The thermal distribution is assumed to be the Maxwell-Jüttner distribution (Jüttner, 1911) with an isotropic temperature. This is the relativistic generalization of the Maxwell-Boltzmann distribution and can be expressed in terms of the Lorentz factor γ as

$$f_\gamma = \frac{\gamma^2\sqrt{1-1/\gamma^2}}{\Theta K_2(1/\Theta)}\exp\left(-\frac{\gamma}{\Theta}\right), \tag{18}$$

where $\Theta = k_B T/mc^2$ is the normalized temperature and K_n is the modified Bessel function of the second kind of order n. This distribution is a considerable simplification, and repercussions of this simplification and possible remedies will be discussed in section 7. Using $\gamma = \sqrt{1+p^2/m^2c^2} = \sqrt{1+\bar{p}^2}$ where $\bar{\mathbf{p}} = \mathbf{p}/mc$ is the normalized particle momentum, Equation 18 can be expressed as

$$f_{\bar{\mathbf{p}}} = \frac{1}{4\pi\Theta K_2(1/\Theta)}\exp\left(-\frac{\sqrt{1+\bar{p}^2}}{\Theta}\right). \tag{19}$$

Integrating Equation 19 in $\bar{p}_z$ and over all angles gives $f_{\bar{p}_\perp}$:

$$f_{\bar{p}_\perp} = \frac{\bar{p}_\perp\sqrt{1+\bar{p}_\perp^2}}{\Theta K_2(1/\Theta)}K_1\left(\frac{\sqrt{1+\bar{p}_\perp^2}}{\Theta}\right). \tag{20}$$

Note that $f_{\bar{\mathbf{p}}}$ is defined in 3D $\bar{\mathbf{p}}$-space so that $\int f_{\bar{\mathbf{p}}} d^3\bar{\mathbf{p}} = 1$, whereas $f_{\bar{p}_\perp}$ is defined in 1D $\bar{p}_\perp$-space so that $\int f_{\bar{p}_\perp} d\bar{p}_\perp = 1$. Integrating Equation 19 in $\bar{p}_x$ and $\bar{p}_y$ gives $f_{\bar{p}_z}$:

$$f_{\bar{p}_z} = \frac{\Theta}{2K_2(1/\Theta)}\left(1+\frac{\sqrt{1+\bar{p}_z^2}}{\Theta}\right)\exp\left(-\frac{\sqrt{1+\bar{p}_z^2}}{\Theta}\right), \tag{21}$$

where $\int f_{\bar{p}_z} d\bar{p}_z = 1$. The details of the derivations of $f_{\bar{p}_\perp}$ and $f_{\bar{p}_z}$ are given in Appendices A and B, respectively.

Now, noting that $\gamma\boldsymbol{\beta} = \gamma\mathbf{v}/c = \mathbf{p}/mc = \bar{\mathbf{p}}$, the mismatch parameter (Equation 5) can be expressed as

$$\xi = 1 + \alpha\left(n\bar{p}_z - \gamma\right). \tag{22}$$

The probability distribution of having a specific ξ is obtained by multiplying the probability distribution of having a certain γ by that of having the corresponding $\bar{p}_z$ which yields the specified ξ, and then integrating over all γ (full derivation given in Appendix C). The solution is

$$f_\xi = \int_1^\infty \frac{\gamma^2\sqrt{1-1/\gamma^2}}{2\alpha n K_2^2(1/\Theta)}\left(1+\frac{\sqrt{1+\bar{p}_z^2(\gamma,\xi)}}{\Theta}\right)\exp\left(-\frac{\gamma+\sqrt{1+\bar{p}_z^2(\gamma,\xi)}}{\Theta}\right)d\gamma, \tag{23}$$

where $\bar{p}_z(\gamma,\xi) = \left[(\xi-1)/\alpha + \gamma\right]/n$ is a rearrangement of Equation 22 and $\int f_\xi d\xi = 1$. Given Θ, α, and n, Equation 23 is an integral solution for f_ξ.

Figure 2 shows f_ξ for different (a) Θ, (b) α, and (c) n values. The default values are $\Theta = 0.1$, $\alpha = 0.25$, and $n = 10$, where $\alpha = 0.25$ and $\Theta = 0.1$ are relevant values for the dayside outer magnetosphere (Tsurutani et al., 2009), and $n = 18 \sim 10$ from the whistler dispersion relation (Equation 28). The black dashed vertical line represents the resonant condition $\xi = 0$ (or equivalently Equation 1). As Θ, α, and n increase from zero, f_ξ broadens and more particles are resonant. After a certain threshold, however, too much broadening leads to the decrease of the local magnitude of f_ξ ($\xi = 0$) and reduces the number of resonant particles. Increasing α significantly changes the mean value of ξ as well, raising this threshold higher.

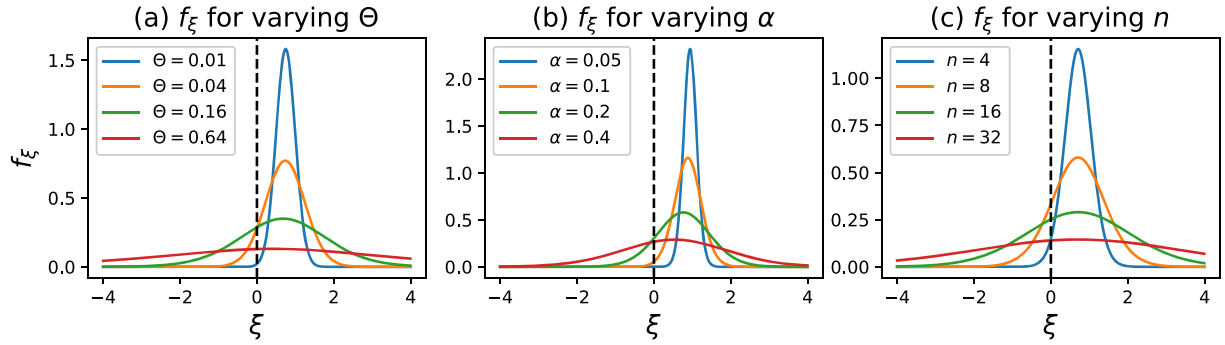

Figure 2. f_ξ for different (a) Θ, (b) α, and (c) n values. The default values are Θ = 0.1, α = 0.25, and n = 10. The black dashed line is the resonant condition $\xi = 0$.

5. Fraction of Particles Undergoing Two-Valley Motion

Before calculating the fraction of particles undergoing two-valley motion, the probability distribution of the limits of integration (Equation 17) must first be derived. Again, the subscript zero will be dropped. From Equation 8, $s = \alpha n \beta_\perp \gamma / \gamma_T = \alpha\sqrt{n^2-1}\bar{p}_\perp$, so the relevant distribution is that of $\bar{p}_\perp$ and $\sin\phi$. Equation 20prescribes $f_{\bar{p}_\perp}$, and assuming that ϕ is isotropic, the probability distribution of $\Phi = \sin\phi$ is the Arcsine(−1,1) distribution,

$$f_\Phi = \frac{1}{\pi\sqrt{1-\Phi^2}}, \tag{24}$$

for $\Phi \in (-1, 1)$.

We now have all the ingredients to calculate the fraction of particles that undergo two-valley motion in ξ-space and thus experience large pitch-angle scattering. This fraction can be found by calculating the probability that both Equations 13 and 16 (i.e., Equation 17) are satisfied. In the case $\Phi > 0$ when Equation 13 is always met, after defining a numerical factor $a = 2\alpha\kappa'\sqrt{n^2-1}$ so that $2s\kappa'\sin\phi = a\bar{p}_\perp\Phi$ and $2s\kappa'(1-\sin\phi) = a\bar{p}_\perp(1-\Phi)$, the probability of two-valley motion is

$$p_+ = \int_{\bar{p}_\perp=0}^{\infty}\int_{\Phi=0}^{1} f_{\bar{p}_\perp} f_\Phi \int_{\xi=-\sqrt{a\bar{p}_\perp(1-\Phi)}}^{\sqrt{a\bar{p}_\perp(1-\Phi)}} f_\xi d\xi d\Phi d\bar{p}_\perp. \tag{25}$$

In the opposite case where $\Phi \le 0$, the probability of two-valley motion is

$$p_- = \int_{\bar{p}_\perp=0}^{\infty}\int_{\Phi=-1}^{0} f_{\bar{p}_\perp} f_\Phi \left(\int_{-\sqrt{a\bar{p}_\perp(1-\Phi)}}^{-\sqrt{-a\bar{p}_\perp\Phi}} f_\xi d\xi + \int_{\sqrt{-a\bar{p}_\perp\Phi}}^{\sqrt{a\bar{p}_\perp(1-\Phi)}} f_\xi d\xi \right) d\Phi d\bar{p}_\perp. \tag{26}$$

The total fraction of particles undergoing two-valley motion is then $p_{tv} = p_+ + p_-$.

There are four degrees of freedom when calculating p_{tv}: Θ, α, n, and κ. However, one degree of freedom can be eliminated by linking α and n through the whistler wave dispersion relation, which, for parallel propagation and $\Omega_p/\Omega \gg 1$ where Ω_p is the electron plasma frequency, is

$$\frac{c^2k^2}{\omega^2} = \frac{\Omega_p^2/\omega^2}{|\Omega|/\omega - 1}. \tag{27}$$

In terms of the dimensionless variables used in this paper, this becomes

$$n = \frac{\Omega_p/\Omega}{\sqrt{\alpha(1-\alpha)}}, \tag{28}$$

which can be used to express $n(\alpha)$ if Ω_p/Ω is specified. Using parameters in Tsurutani et al. (2009) ($n_e \simeq 10\,\mathrm{cm}^{-3}$, $B_0 \simeq 125\,\mathrm{nT}$), we obtain $\Omega_p/\Omega \simeq 8$; this value will be used throughout the rest of the analysis.

Let us now calculate p_{tv} for the parameters in the range $0.0001 \le \kappa \le 0.01$, $0.1 \le \alpha \le 0.8$, and $0.01 \le \Theta \le 10$ (corresponding to electron thermal energies from 5.11 keV to 5.11 MeV). Since the parameter range is determined, the conditions for which the assumption $\kappa' \ll s^3$ that was used to derive Equation 17

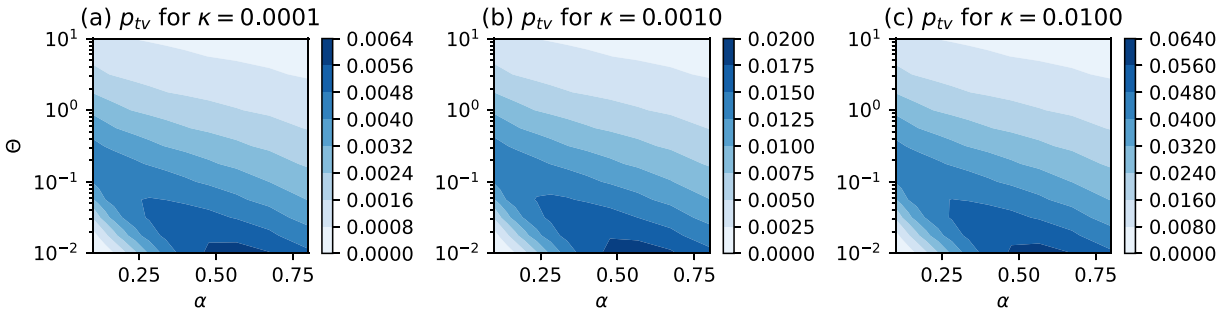

Figure 3. p_{tv} as a function of α and Θ for different κ values.

is true can now be determined. Because $n \gg 1$, $\kappa' = \kappa/\gamma_T = \kappa\sqrt{1-1/n^2} \simeq \kappa$ and $s = \alpha\sqrt{n^2-1}\bar{p}_\perp \simeq \alpha n \bar{p}_\perp$. From Equation 28 it follows that $\alpha n = \left(\Omega_p/\Omega\right)\sqrt{\alpha/(1-\alpha)}$. We now compare the largest value of κ to the lowest value of s^3, which involves the smallest values of α and Θ. For $\Theta \ll 1$, the most likely $\bar{p}_\perp$ is $\sqrt{\Theta}$ (see Appendix D). Thus, the condition $\kappa' \ll s^3$ can be expressed as $\kappa \ll \left(\left(\Omega_p/\Omega\right)\sqrt{\alpha\Theta/(1-\alpha)}\right)^3$, or $\Theta \gg \kappa^{2/3}/\left[\left(\Omega_p/\Omega\right)^2(\alpha/(1-\alpha))\right]$. Inserting $\alpha = 0.1$ and $\kappa = 0.01$ shows that $\kappa' \ll s^3$ is valid if $\Theta \gg 0.0066$. Thus, $0.01 \leq \Theta \leq 10$ is consistent with $\kappa' \ll s^3$.

Figure 3 shows contours of p_{tv} as a function of α and Θ for different κ values. For $\kappa \geq 0.001$, which is typical for magnetospheric chorus (Macúšová et al., 2015; Tsurutani et al., 2009), a significant fraction (1%–5%) of particles undergo two-valley motion and thus large pitch-angle scattering. However, p_{tv} decreases at high Θ ($\Theta \gtrsim 1$), and this phenomenon is related to the decrease of the local magnitude of f_ξ ($\xi = 0$) if there is too much broadening of f_ξ, as shown in Figure 2. Figure 3 also shows that $p_{tv}(\alpha, \Theta)$ has more or less the same shape across a wide range of κ but its magnitude is proportional to $\sqrt{\kappa}$. This is because the limits of the ξ integrals in Equations 25 and 26 scale as $\sqrt{a} \sim \sqrt{\kappa}$, so if the integration range is sufficiently small so that the integrand may be approximated by a linear function, it follows that $p_{tv} \propto \sqrt{\kappa}$.

6. Numerical Verification

The analytical predictions presented in this paper will now be verified via numerical simulations. A computer code was written, which solves Equation 4 and $d\mathbf{x}/dt = c\boldsymbol{\beta}$ using the fully implicit Runge-Kutta method of the Radau IIA family of order 5 (Hairer & Wanner, 1991) in the scipy.integrate.solve_ivp package in Python 3.7. This particular method was used because it yielded the smallest numerical error out of the available methods in the Python package, measured by the drift of the average value of the pitch-angle over the full simulation time. This drift should be zero in principle because the coefficients of $\psi(\xi)$ are time-independent, but numerical error introduces a small drift. For example, the simulations in Figures 1c and 1d show that the particles' pitch-angles undergo oscillatory motion, but there are ever-so-slight, almost unnoticeable drifts ($\lesssim 0.1°$) of the average values. The error was quantified by using the statistics of the 10,000 particles in Figure 5c. The Radau method with a time step $\Delta t = 0.2$ yielded a median value for the pitch-angle drift of 0.07° with a standard deviation of 0.14°, which is far smaller than the pitch-angle oscillation of a vast majority of the particles. The simulation time was set long enough for every particle to undergo at least several oscillations in the pitch-angle. The electromagnetic fields were prescribed by Equations 2 and 3, which is a simplified model of a whistler wave. The code was parallelized with the multiprocessingpackage.

It will first be verified that particles that satisfy Equation 17 and thus undergo two-valley motion experience large pitch-angle scattering. 2,500 particle trajectories were numerically integrated, and the initial particle momenta were scanned in the range $\bar{p}_\perp \in [0, 2]$, $\bar{p}_z \in [-0.5, 0]$, and $\phi = \pi/4, -\pi/4$. The wave amplitude was $\kappa = 0.005$, and the wave frequency was $\alpha = 0.25$, which gives $n = 18$ using Equation 28.

Figure 4a shows the regions of initial momentum space (dark green) that satisfy the unapproximated two-valley criteria (Equations 14 and $b < 0$) for $\phi = \pi/4$. Figure 4b shows regions of this space that satisfy the approximated criterion (Equation 17). The regions are virtually identical except for $\bar{p}_\perp \lesssim 0.1$ because for sufficiently large $\bar{p}_\perp$, the $\kappa \ll s^3$ approximation holds. Figures 4a and 4b are effectively predictions of large pitch-angle scattering. The colors in Figure 4c show the pitch-angle range that a particle undergoes for

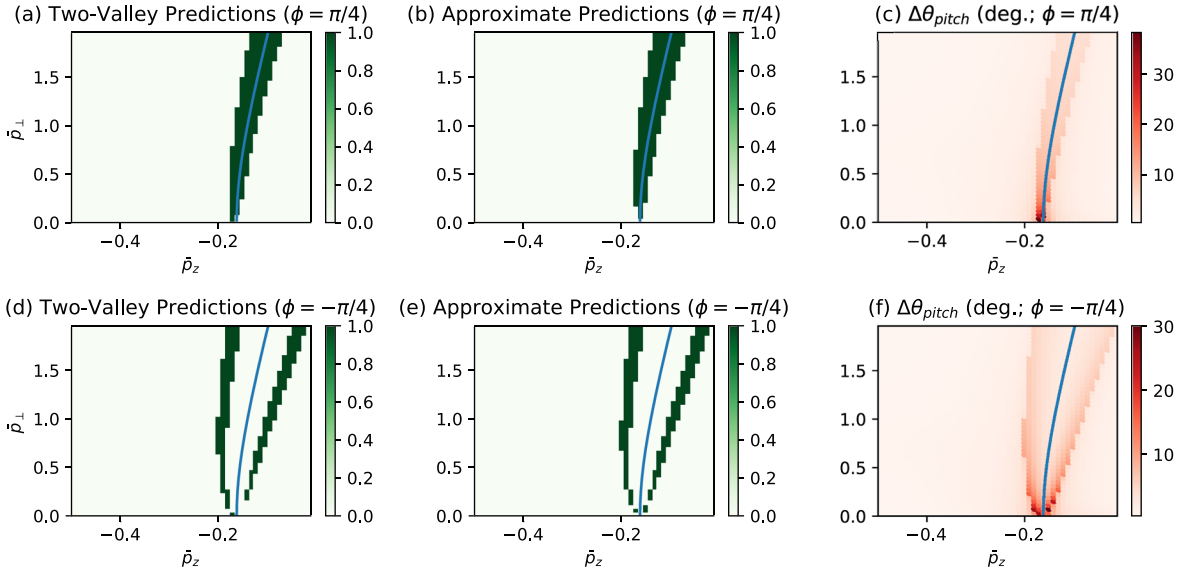

Figure 4. (a) Regions of initial momentum space (dark green) that satisfy the unapproximated two-valley criteria (Equations 14 and $b < 0$) for $\phi = \pi/4$. (b) Regions of this space that satisfy the approximated criterion (Equation 17) for $\phi = \pi/4$. (c) Pitch-angle range (in degrees) within a single particle trajectory for a range of initial particle momenta for $\phi = \pi/4$. Panels (d)–(f) are the same as Panels (a)–(c) except for $\phi = -\pi/4$. Blue lines represent the resonance condition (Equation 1; $\xi = 0$). The wave parameters were $\alpha = 0.25$, $\kappa = 0.005$, and $n = 18$ from Equation 28.

each point in $(\bar{p}_\perp, \bar{p}_z)$ space; this pitch-angle range is defined by the absolute difference between the maximum and minimum pitch-angles along the particle trajectory. For example, the particle in Figure 1c has a pitch-angle range of ∼15°, and that in Figure 1d has a pitch-angle range of ∼3°. Figures 4d–4f are the same as Figures 4a–4c except for $\phi = -\pi/4$. It can be clearly seen that if a particle's initial momentum satisfies the two-valley criteria, it undergoes a large pitch-angle scattering.

The blue curves in Figure 4 represent the resonance condition (Equation 1; $\xi = 0$). The curve is found by solving $\xi = 1 + \alpha(n\bar{p}_z - \gamma) = 1 + \alpha(n\bar{p}_z - \sqrt{1 + \bar{p}_\perp^2 + \bar{p}_z^2}) = 0$ for $\bar{p}_\perp(\bar{p}_z)$ and restricting the domain of $\bar{p}_z$ to be consistent with $\gamma = \alpha^{-1} + n\bar{p}_z \geq 1$. In Figures 4d–4f, the blue lines do not pass through regions of two-valley motion and large scattering. This fact is consistent with Equation 17, which qualitatively states that for $\phi < 0$, the condition for two-valley motion and large scattering does not include $\xi = 0$.

Next, the analytical prediction for p_{tv} will be verified via the Monte-Carlo method. The trajectories of 10,000 particles whose initial momenta were randomly sampled from Equation 19 were respectively integrated for $\kappa = 0.0001, 0.001$ and 0.01. Other parameters were $\alpha = 0.25$, $n = 18$, and $\Theta = 0.1$.

Figure 5 shows the pitch-angle range (in degrees) of the randomly sampled particles for different κ values. Red points represent particles that meet the two-valley criterion (Equation 17), and the text inside represents the percentage of red particles. Figure 3 shows that for $\alpha = 0.25$ and $\Theta = 0.1$, the predicted percentage ranges

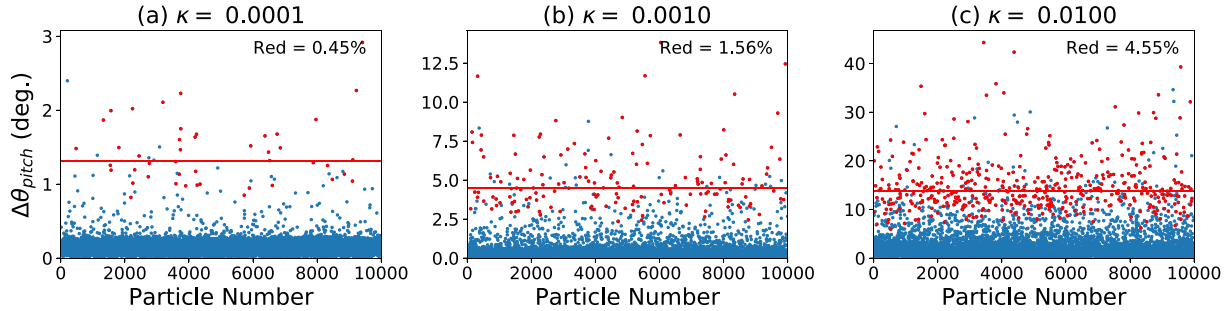

Figure 5. Pitch-angle range of 10,000 particles whose initial momenta were randomly sampled from Equation 19 for different κ values. Red points represent particles that meet the two-valley criterion (Equation 17), and the text inside represents the percentage of red particles. The red horizontal lines represents the median $\Delta\theta_{pitch}$ of the red particles in degrees.

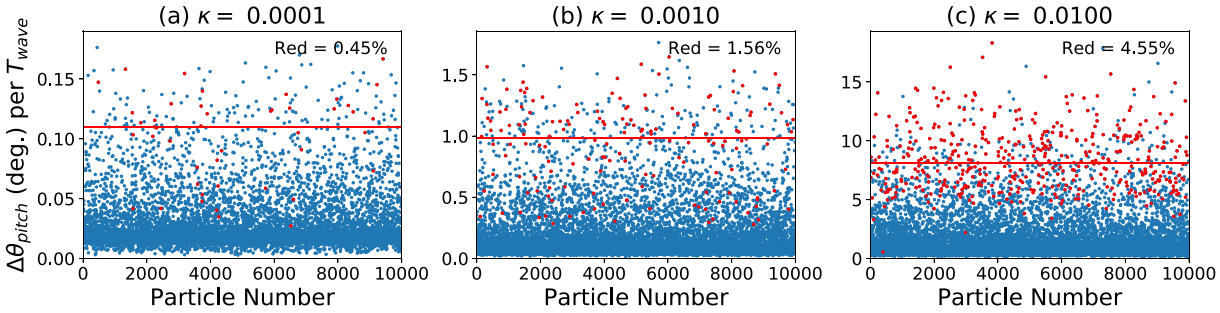

Figure 6. Pitch-angle change per wave period of the respective simulations in Figure 5. The red horizontal lines, respectively, represent the median value of the pitch-angle change per wave period of the red particles.

are 0.4–0.48%, 1.25–1.5%, and 4.00–4.80% for $\kappa = 0.0001, 0.001$, and 0.01, respectively, which approximately agree with the results in Figure 5. Red points generally experience significantly larger pitch-angle scattering than other particles, as can be seen from the median value of the red points (red horizontal lines). However, it can be seen that there are blue points that also experience large scattering; examining the pseudo-potential $\psi(\xi)$ for these points shows that these particles have pseudo-energies that are just short of overcoming the two-valley hill, so they "almost" undergo two-valley motion and experience substantial pitch-angle scattering. Therefore, we conclude that p_{tv} is a lower-bound for the fraction of particles with large pitch-angle scattering.

Even if two-valley motion were to cause large pitch-angle scattering, the mechanism would not be significant if this scattering could not occur within a short enough time. Thus, it is necessary to show that the coherent wave lasts sufficiently long for two-valley motion to occur. Figure 6 shows the pitch-angle change within a single wave period for the respective simulations in Figure 5. Tsurutani et al. (2009) observed in the outer magnetosphere coherent chorus elements with amplitudes $\kappa \simeq 0.0016$ ($B_0 \simeq 125$ nT and wave field $\tilde{B} \simeq 200$ pT) that are 0.1∼0.5 s long with a frequency of ∼700 Hz. These elements consisted of subelements or packets lasting 5∼10 ms, corresponding to about 3.5 to 7 wave periods. $\kappa \simeq 0.0016$ approximately corresponds to Figure 6b, which shows that red particles can reach their median pitch-angle range (∼5° from Figure 5b) in five wave periods on average. For $\kappa = 0.01$ (Figure 6b), this rate is even faster as the red particles can reach their median pitch-angle range of ∼ 15° (Figure 5c) in about two wave periods.

7. Discussion

The results presented here may help explain the association of large-amplitude whistler waves to relativistic microbursts (∼1 MeV) (Breneman et al., 2017) and may explain the lack of such energetic microbursts in small-amplitude chorus (Tsurutani et al., 2013). Particle energization is not a subject of this paper and thus will not be discussed; it will be assumed that the particles are first energized by some mechanism that yields a relativistic distribution, and then the ensuing pitch-angle dynamics are studied in order to concentrate on one topic. It should be noted, however, that energization and pitch-angle scattering may occur simultaneously.

In Figure 3, for small amplitudes ($0.0001 \leq \kappa \leq 0.001$), only up to 0.5% of particles in a distribution with a temperature of ∼1 MeV (corresponding to $\Theta \simeq 2$) interact with the wave, whereas for large amplitudes ($\kappa \simeq 0.01$), ∼2% of such particles do. This is because the range of the two-valley condition in Equation 17 scales with the wave amplitude κ; that is, as the wave amplitude increases, more particles, including energetic particles, satisfy the two-valley condition.

The interaction of large-amplitude waves with relativistic particles is further explained in Figure 7, which is the same as Figure 4 but for a larger wave amplitude ($\kappa = 0.02$). It can clearly be seen that the predictions of large scattering in Figure 7 are much broader in phase space than those in Figure 4. This is important because in Figure 4, relativistic particles with $\bar{p} \gtrsim 1$ must have large initial pitch-angles to interact with the wave since the two-valley condition is a narrow range related to the exact resonance condition, and thus, these particles must undergo extremely large pitch-angle scatterings in order to jump into the loss cone. However, in Figure 7, the range for two-valley motion is much increased, allowing for relativistic particles with smaller

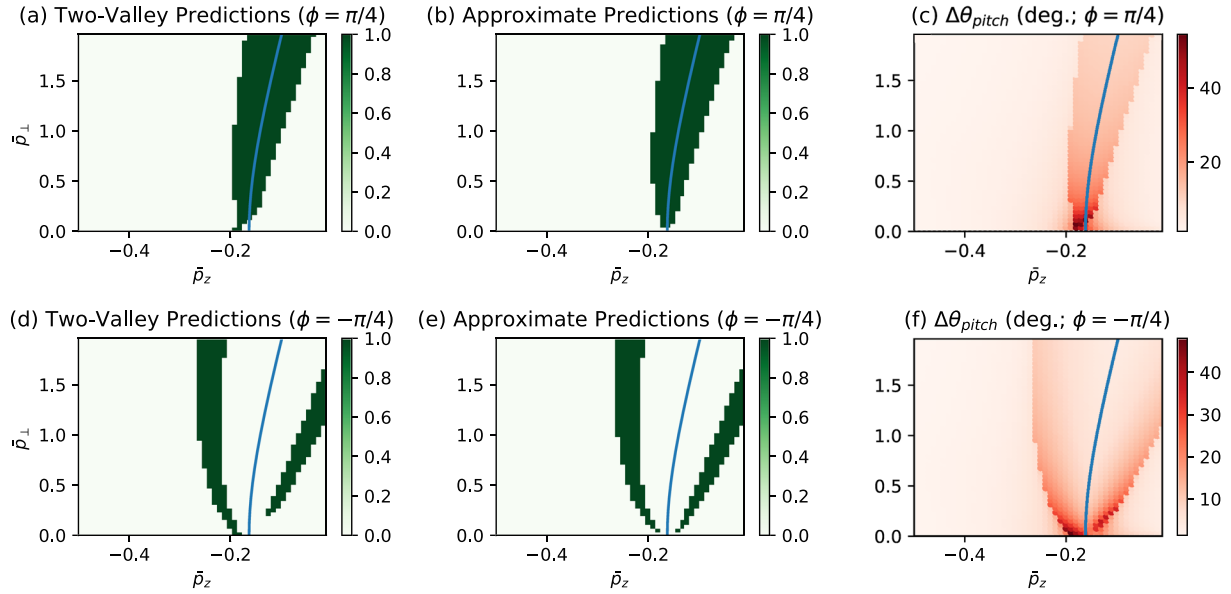

Figure 7. Same as Figure 4, but for $\kappa = 0.02$.

initial pitch-angles to interact with the wave. The deviation of the two-valley condition from the exact resonance condition is because the range in Equation 17 scales with κ. Furthermore, the pitch-angle range itself is significantly increased in Figure 7. Therefore, a larger wave amplitude allows for relativistic particles with lower initial pitch-angles to interact with the wave, while simultaneously increasing the amount of pitch-angle scattering; these two effects lead to more relativistic particles being pitch-angle scattered into the loss-cone.

There are a few limitations to the present analysis that may be subject to future work. First, the Maxwell-Jüttner distribution is a simplification and should not be considered as a distribution representing the entire electron population. The actual distribution is a sum of these Maxwellians or other functions such as the kappa distribution (Pierrard & Lazar, 2010). If the actual distribution can be expressed as a weighted sum of Maxwelll-Jüttner distributions, then the total fraction of particles that undergo two-valley motion is the sum of the partial fractions for each distribution. On the other hand, if the actual distribution is another sufficiently simple function, then an analysis similar to that in sections 4 and 5 may be conducted by replacing Equation 18 by the actual distribution. However, depending on the complexity of the actual distribution, its transition to f_ξ may be more complicated.

Second, the particle temperature is assumed for simplicity to be isotropic, whereas observations indicate that electron temperature in the magnetosphere in general is anisotropic and electron distribution functions can be more complex than simple anisotropic distributions (Li et al., 2010). The transition to an anisotropic Maxwell-Jüttner distribution is outlined in Livadiotis (2016) and Treumann and Baumjohann (2016).

Third, the wave is assumed to have exact parallel propagation, whereas many instances of magnetospheric chorus involve oblique propagation (Artemyev et al., 2016; Santolík et al., 2009). Also, chorus typically exhibits frequency and amplitude changes over a short time period (Tsurutani et al., 2009), but the model presented here is based on a plane wave with a fixed frequency and wavenumber (Equations 2 and 3). However, including obliquity and variable frequency makes the analysis considerably more complicated and so would be inappropriate for an inaugural analysis.

8. Comparison to Second-Order Trapping Theory

A popular theory describing wave-particle interactions is the second-order trapping effect presented in, for example, Sudan and Ott (1971), Nunn (1974), and Omura et al. (1991). Omura et al. (2007, 2008) present relativistic generalizations of the theory. However, it will now be shown that this previous theory is an approximation of the theory presented here; this approximation effectively misses the critical two-valley nature of the pseudo-potential.

Omura et al. (1991) use the following coupled equations for nonrelativistic speeds:

$$\frac{d\zeta}{dt} = k(v_z - V_R), \tag{29}$$

$$\frac{d}{dt}(v_z - V_R) = \frac{\omega_t^2}{k}(\sin\zeta + S), \tag{30}$$

where

$$V_R = \frac{\omega - \Omega}{k}, \tag{31}$$

ζ is the angle between $\mathbf{v}_\perp$ and $\tilde{\mathbf{B}}$, $\omega_t = \sqrt{kv_\perp \Omega\kappa}$ is the trapping frequency, and S is a parameter that is equal to zero when the background magnetic field is spatially uniform and ω is a constant. Therefore, setting $S = 0$, differentiating Equation 30 in time, and using Equation 29,

$$\frac{d^2}{dt^2}(v_z - V_R) = \frac{\omega_t^2}{k}\cos\zeta\frac{d\zeta}{dt}, \tag{32}$$

$$= \omega_t^2(v_z - V_R)\cos\zeta. \tag{33}$$

Letting $\gamma = 1$ in Equation 5 and rearranging shows that

$$\xi = \frac{k}{\Omega}\left(v_z - V_R\right), \tag{34}$$

so Equation 33 becomes

$$\frac{d^2\xi}{dt^2} = \xi\omega_t^2\cos\zeta, \tag{35}$$

$$= -\frac{\partial}{\partial\xi}\left(-\frac{\xi^2}{2}\omega_t^2\cos\zeta\right), \tag{36}$$

$$\frac{1}{\Omega^2}\frac{d^2\xi}{dt^2} = -\frac{\partial\chi(\xi)}{\partial\xi}, \tag{37}$$

where $\chi(\xi) = -\xi^2\omega_t^2\cos\zeta/2\Omega^2$ is the pseudo-potential of this system.

Now, let us examine the term involving $s\kappa'$ in Equation 7 assuming $\gamma_0 = \gamma_T = 1$;

$$-s\kappa\sin\phi_0\frac{\xi^2}{2} = -\alpha n\kappa\beta_{\perp 0}\sin\phi_0\frac{\xi^2}{2}, \tag{38}$$

$$= -\frac{\omega}{\Omega}\frac{ck}{\omega}\kappa\frac{v_{\perp 0}}{c}\sin\phi_0\frac{\xi^2}{2}, \tag{39}$$

$$= -\frac{\omega_{t0}^2}{\Omega^2}\sin\phi_0\frac{\xi^2}{2}, \tag{40}$$

$$= \chi_0(\xi), \tag{41}$$

because ζ and ϕ are related by $\zeta = \phi - \pi/2$, so $\cos\zeta = \sin\phi$. $\chi_0(\xi)$ is $\chi(\xi)$ except that $v_{\perp 0}$ and ϕ_0 are used instead of $v_\perp$ and ϕ, and the relationship is similar for ω_{t0} and ω_t. Therefore, $\chi(\xi)$ results from keeping only the $s\kappa'$ term in $\psi(\xi)$. This is important because $\chi(\xi)$ only describes either a trapping or a nontrapping potential but not a two-valley potential.

Figures 1e and 1f plot the approximated pseudo-potentials $\chi(\xi)$ for the particles in Figures 1a and 1b, respectively. For both particles, $\chi(\xi)$ is clearly a one-valley potential, whereas the unapproximated $\psi(\xi)$ is two-valleyed for the particle in Figure 1a, and thus, it undergoes much larger pitch-angle scattering than the particle in Figure 1b. Therefore, if the theory in Omura et al. (1991) were to be used, it would be impossible to distinguish between the two particles that clearly have an extremely large difference in the amount of pitch-angle scattering.

Another important problem with the second-order trapping theory is that the time-dependence of the variables is ambiguous at best. Omura et al. (1991) imply that $v_\perp$ and thus ω_t are time-dependent but then treat $v_\perp$ as a constant when they state that combining Equations 29 and 30 gives a pendulum equation. Sudan and Ott (1971) admit that $v_\perp$ is time-dependent, but then argue that it can be treated as a constant, as specified

in the sentence after their equation 10. In the present theory, however, we explicitly differentiate between the initial variables and the time-dependent ones, so no approximation regarding time-dependence needs to be made. This is an extremely important point because this time-dependence of $v_\perp$ gives the two-valley potential whereas treating it as a constant does not. This fact can be more explicitly illustrated by examining equation 26 in Bellan (2013), which is an equation for the parallel velocity (recall that $\beta_z = v_z/c$ and prime refers to the wave frame):

$$\frac{1}{\Omega'}\frac{d^2\beta'_z}{dt'^2} = \xi\boldsymbol{\beta}'_\perp \cdot \frac{\tilde{\mathbf{B}}'_\perp}{B_0} - \beta'_z \frac{\tilde{\mathbf{B}}'_\perp}{B_0}\cdot\frac{\tilde{\mathbf{B}}'_\perp}{B_0}. \tag{42}$$

The second-order trapping theory effectively drops the last term in Equation 42 and ignores the time-dependence of the first term on the right-hand side. This leads to

$$\frac{1}{\Omega'}\frac{d^2\xi}{dt'^2} = \alpha n\frac{\gamma'}{\gamma_T}\xi\boldsymbol{\beta}'_\perp \cdot \frac{\tilde{\mathbf{B}}'_\perp}{B_0}, \tag{43}$$

which is equivalent to Equation 37 if $\gamma' = \gamma_T = 1$ is assumed. However, equation 35 of Bellan (2013) states that

$$\boldsymbol{\beta}'_\perp \cdot \frac{\tilde{\mathbf{B}}'_\perp}{B_0} = \boldsymbol{\beta}'_{\perp 0}\cdot\frac{\tilde{\mathbf{B}}'_{\perp 0}}{B_0} - \frac{\gamma_T}{2\alpha n\gamma'}\left(\xi^2 - \xi_0^2\right), \tag{44}$$

which means that treating $v_\perp$ as a constant effectively misses the ξ-dependence in Equation 44, which is the reason for the two-valley shape of the pseudo-potential.

For example, neglecting the ξ_0^2 term in Equation 44 leads to erroneous conclusions regarding the shape of the potential near $\xi = 0$. In Figure 1e, $\chi(\xi)$ is a valley because $-s\kappa'\sin\phi_0$ is positive in this case. However, the correct pseudo-potential $\psi(\xi)$ in Figure 1a is a hill near $\xi = 0$ because $-\xi_0^2/2 - s\kappa'\sin\phi_0$ in Equation 7 is negative in this case. Also, the ξ^2 term in Equation 44, which leads to the positive ξ^4 term in Equation 7, prevents the pseudo-potential from diverging to $-\infty$ as $\xi \to \pm\infty$. This prevents the particle ξ from veering off to infinity; this phenomenon is unphysically allowed if the approximated $\chi(\xi)$ is used and $\sin\phi_0 > 0$. The term linear in ξ in Equation 7, which affects the asymmetry of the two-valleys is also neglected in $\chi(\xi)$. The fact that $v_\perp$ is not constant can be explicitly seen in figure 5g of Bellan (2013), where $v_\perp$ of a particle undergoing two-valley motion varies in time by over a factor of three.

It should be noted, however, that for a nonuniform background field and/or time-dependent wave frequencies, S is finite in Equation 30 and this may have an important role in the system additional to the effects described in the present paper. In fact, many studies that use the approximated second-order trapping theory focus on the nonlocal processes where effects due to finite S are significant (e.g., in Omura et al., 2007). The present study focuses on local scattering that happens over only a few wave periods, so S can be presumed to be small, and $\psi(\xi)$ instead of $\chi(\xi)$ must be used.

A simple way to see that S is locally negligible is to consider the physical length of the wave for the duration of the pitch-angle scattering. From Figures 5 and 6, maximum deflection happens within five wave periods. For $B_0 = 125$ nT, $\Omega = 2.2\times10^4$ rad/s. Using the wave parameters that have been used so far, $\alpha = 0.25$ gives $\omega = 5.5\times10^3$ rad/s, and $n = 18$ gives the wavelength to be $\lambda = 19$ km. Therefore, five wave periods correspond to about 100 km, which is a minuscule distance compared to the length scale of the magnetosphere at $L \simeq 5$ where plentiful amounts of relativistic microbursts occur (Tsurutani et al., 2013). The time-dependence of the wave frequency is also negligible because a single chorus element lasts for around 0.1–0.5 s while its frequency increases by about 50%, but five wave periods corresponds to less than 0.01 s (Tsurutani et al., 2009). Therefore, S can be considered to be negligible during the local scattering process.

9. Conclusion

The interaction of a relativistically consistent thermal distribution of particles with a coherent right-handed circularly polarized wave has been investigated. Departure from wave-particle resonance for each particle is expressed by a frequency mismatch parameter ξ, where $\xi = 0$ represents perfect resonance. An exact rearrangement of the relativistic particle equation of motion shows that ξ follows pseudo-Hamiltonian dynamics with an associated pseudo-potential $\psi(\xi)$. If $\psi(\xi)$ has two-valleys separated by a hill, and the particle has enough pseudo-energy to overcome the hill, then the particle undergoes two-valley ξ-space motion that produces a large, nondiffusive pitch-angle scattering.

An accurate condition for two-valley motion and thus for large pitch-angle scattering has been derived; this condition is related to but may or may not include the exact resonance condition (Equation 1), and the range of this condition scales with the wave amplitude. Assuming that the particle distribution is Maxwell-Jüttner, which is a relativistic generalization of the Maxwell-Boltzmann distribution, for typical magnetospheric parameters a significant fraction (1–5%) of the particles undergoes two-valley motion. The pertinent analysis can potentially be used for the actual local electron distribution, which may not be exactly Maxwellian. Numerical simulations confirm the analytical results. The scaling of the fraction of interacting particles with the wave amplitude may also explain the association of relativistic microbursts to large-amplitude chorus. The present theory is more accurate and exact than the widely used second-order trapping theory as second-order trapping theory fails to take into account two-valley motion.

Appendix A: Derivation of $f_{\bar{p}_\perp}$

In cylindrical coordinates, Equation 19 is equivalent to

$$f_{\bar{\mathbf{p}}} d^3\bar{\mathbf{p}} = \frac{1}{4\pi\Theta K_2(1/\Theta)} \exp\left(-\frac{\sqrt{1+\bar{p}^2}}{\Theta}\right) \bar{p}_\perp d\bar{p}_\perp d\phi d\bar{p}_z. \tag{A1}$$

Integrating in $\bar{p}_z$ gives

$$\int_{\bar{p}_z=-\infty}^{\infty} f_{\bar{\mathbf{p}}} \bar{p}_\perp d\bar{p}_\perp d\phi d\bar{p}_z = \int_{\bar{p}_z=-\infty}^{\infty} \frac{1}{4\pi\Theta K_2(1/\Theta)} \exp\left(-\frac{\sqrt{1+\bar{p}_\perp^2+\bar{p}_z^2}}{\Theta}\right) \bar{p}_\perp d\bar{p}_\perp d\phi d\bar{p}_z \tag{A2}$$

$$= \bar{p}_\perp d\bar{p}_\perp d\phi \int_{\bar{p}_z=0}^{\infty} \frac{1}{2\pi\Theta K_2(1/\Theta)} \exp\left(-\frac{\sqrt{1+\bar{p}_\perp^2+\bar{p}_z^2}}{\Theta}\right) d\bar{p}_z, \tag{A3}$$

where $\bar{p}^2 = \bar{p}_\perp^2 + \bar{p}_z^2$. Defining

$$a^2 = \frac{1+\bar{p}_\perp^2}{\Theta^2} \tag{A4}$$

and

$$t = \frac{\bar{p}_z}{\Theta}, \tag{A5}$$

the $\bar{p}_z$-integral in Equation A3 becomes

$$\frac{1}{2\pi K_2(1/\Theta)} \int_0^\infty \exp\left(-\sqrt{a^2+t^2}\right) dt. \tag{A6}$$

Now we define

$$t = a\sinh z, \tag{A7}$$

so $\sqrt{a^2+t^2} = a\sqrt{1+\sinh^2 z} = a\cosh z$ and $dt = a\cosh z dz$. Equation A6 is now

$$\frac{a}{2\pi K_2(1/\Theta)} \int_0^\infty \cosh z \exp(-a\cosh z)\, dz. \tag{A8}$$

The z-integral in Equation A8 evaluates to $K_1(a)$ where K_n is the modified Bessel function of the second kind of order n (Jeffrey & Zwillinger, 2015, Section 8.432, 1.).

Therefore, Equation A3 is now

$$\frac{\sqrt{1+\bar{p}_\perp^2}}{2\pi\Theta K_2(1/\Theta)} K_1\left(\frac{\sqrt{1+\bar{p}_\perp^2}}{\Theta}\right) \bar{p}_\perp d\bar{p}_\perp d\phi. \tag{A9}$$

Integrating in ϕ yields the final result:

$$f_{\bar{p}_\perp} d\bar{p}_\perp = \frac{\bar{p}_\perp \sqrt{1+\bar{p}_\perp^2}}{\Theta K_2(1/\Theta)} K_1\left(\frac{\sqrt{1+\bar{p}_\perp^2}}{\Theta}\right) d\bar{p}_\perp, \tag{A10}$$

which is Equation 20.

Appendix B: Derivation of $f_{\bar{p}_z}$

In cylindrical coordinates, Equation 19 is equivalent to

$$f_{\bar{\mathbf{p}}} d^3\bar{\boldsymbol{p}} = \frac{1}{4\pi\Theta K_2(1/\Theta)} \exp\left(-\frac{\sqrt{1+\bar{p}^2}}{\Theta}\right) \bar{p}_\perp d\bar{p}_\perp d\phi d\bar{p}_z. \tag{B1}$$

Integrating in all ϕ and $\bar{p}_\perp$, Equation B1 becomes

$$f_{\bar{p}_z} d\bar{p}_z = \int_{\bar{p}_\perp=0}^{\infty} \frac{1}{2\Theta K_2(1/\Theta)} \exp\left(-\frac{\sqrt{1+\bar{p}_\perp^2+\bar{p}_z^2}}{\Theta}\right) \bar{p}_\perp d\bar{p}_\perp d\bar{p}_z. \tag{B2}$$

Letting $\eta^2 = 1+\bar{p}_\perp^2+\bar{p}_z^2$ while keeping $\bar{p}_z$ constant so that

$$\eta d\eta = \bar{p}_\perp d\bar{p}_\perp, \tag{B3}$$

we have

$$f_{\bar{p}_z} d\bar{p}_z = \int_{\eta=\sqrt{1+\bar{p}_z^2}}^{\infty} \frac{1}{2\Theta K_2(1/\Theta)} \exp\left(-\frac{\eta}{\Theta}\right) \eta d\eta d\bar{p}_z. \tag{B4}$$

Using the integral formula (Jeffrey & Zwillinger, 2015, Section 3.351, 2.)

$$\int_u^\infty x^n e^{-\mu x} dx = e^{-u\mu} \sum_{k=0}^{n} \frac{n!}{k!} \frac{u^k}{\mu^{n-k+1}}, \tag{B5}$$

where $x=\eta$, $u=\sqrt{1+\bar{p}_z^2}$, $\mu = 1/\Theta$, and $n=1$ in this case, we have

$$f_{\bar{p}_z} d\bar{p}_z = \frac{1}{2\Theta K_2(1/\Theta)} \left(\Theta^2 + \Theta\sqrt{1+\bar{p}_z^2}\right) \exp\left(-\frac{\sqrt{1+\bar{p}_z^2}}{\Theta}\right), \tag{B6}$$

$$= \frac{\Theta}{2K_2(1/\Theta)} \left(1+\frac{\sqrt{1+\bar{p}_z^2}}{\Theta}\right) \exp\left(-\frac{\sqrt{1+\bar{p}_z^2}}{\Theta}\right), \tag{B7}$$

which is Equation 21.

Appendix C: Derivation of f_ξ

ξ is defined as

$$\xi = 1+\alpha\left(n\bar{p}_z - \gamma\right) = 1+\alpha\zeta, \tag{C1}$$

where $\zeta = n\bar{p}_z - \gamma$.

f_ζ will first be derived. Defining $R = n\bar{p}_z$ (so $d\bar{p}_z = dR/n$ and $\zeta = R-\gamma$), we have

$$f_{\bar{p}_z}(\bar{p}_z) d\bar{p}_z = f_{\bar{p}_z}(R/n) \frac{dR}{n} \tag{C2}$$

$$= \frac{\Theta}{2nK_2(1/\Theta)}\left(1+\frac{\sqrt{1+R^2/n^2}}{\Theta}\right)\exp\left(-\frac{\sqrt{1+R^2/n^2}}{\Theta}\right)dR \tag{C3}$$

$$= f_R(R)dR. \tag{C4}$$

Now, in order for $\zeta = R-\gamma$ to be true, the value of R has to equal $\zeta+\gamma$ for a given value of γ. The probability distribution of this occurrence integrated over all values of γ gives f_ζ:

$$f_\zeta(\zeta) = \int_1^\infty f_\gamma(\gamma) f_R(\zeta+\gamma)\, d\gamma \tag{C5}$$

$$= \int_1^\infty \frac{\gamma^2\sqrt{1-1/\gamma^2}}{2nK_2^2(1/\Theta)}\left(1+\frac{\sqrt{1+(\zeta+\gamma)^2/n^2}}{\Theta}\right)\exp\left(-\frac{\gamma+\sqrt{1+(\zeta+\gamma)^2/n^2}}{\Theta}\right)d\gamma. \tag{C6}$$

Finally, rearranging Equation C1 yields $\zeta(\xi) = (\xi-1)/\alpha$ so that $d\zeta = d\xi/\alpha$. It follows that

$$f_\zeta(\zeta)d\zeta = f_\zeta([\xi-1]/\alpha)\frac{d\xi}{\alpha} \tag{C7}$$

$$= \int_1^\infty \frac{\gamma^2\sqrt{1-1/\gamma^2}}{2\alpha nK_2^2(1/\Theta)}\left(1+\frac{\sqrt{1+(\zeta(\xi)+\gamma)^2/n^2}}{\Theta}\right)\exp\left(-\frac{\gamma+\sqrt{1+(\zeta(\xi)+\gamma)^2/n^2}}{\Theta}\right)d\gamma d\xi \tag{C8}$$

$$= f_\xi(\xi)d\xi. \tag{C9}$$

Writing $\bar{p}_z(\gamma,\xi) = (\zeta(\xi)+\gamma)/n$ yields a more compact expression:

$$f_\xi(\xi) = \int_1^\infty \frac{\gamma^2\sqrt{1-1/\gamma^2}}{2\alpha nK_2^2(1/\Theta)}\left(1+\frac{\sqrt{1+\bar{p}_z^2(\gamma,\xi)}}{\Theta}\right)\exp\left(-\frac{\gamma+\sqrt{1+\bar{p}_z^2(\gamma,\xi)}}{\Theta}\right)d\gamma, \tag{C10}$$

which is Equation 23.

Appendix D: Derivation of Nonrelativistic $f_{\bar{p}_\perp}$

From Equation A10,

$$f_{\bar{p}_\perp} = \frac{\bar{p}_\perp\sqrt{1+\bar{p}_\perp^2}}{\Theta K_2(1/\Theta)}K_1\left(\frac{\sqrt{1+\bar{p}_\perp^2}}{\Theta}\right). \tag{D1}$$

For $\bar{p}_\perp \ll 1$,

$$\sqrt{1+\bar{p}_\perp^2} \simeq 1+\frac{\bar{p}_\perp^2}{2} \tag{D2}$$

For $\Theta \ll 1$, it is seen that (Watson, 1995, Section 7.23)

$$K_2(1/\Theta) \simeq \sqrt{\frac{\pi\Theta}{2}}e^{-1/\Theta}, \tag{D3}$$

and for small $\Theta \ll 1$ and $\bar{p}_\perp \ll 1$,

$$K_1\left(\frac{\sqrt{1+\bar{p}_\perp^2}}{\Theta}\right) \simeq K_1\left(\frac{1}{\Theta}+\frac{\bar{p}_\perp^2}{2\Theta}\right) \tag{D4}$$

$$\simeq \sqrt{\frac{\pi\Theta}{2+\bar{p}_\perp^2}} \exp\left(-\frac{1}{\Theta} - \frac{\bar{p}_\perp^2}{2\Theta}\right), \tag{D5}$$

so to lowest order,

$$f_{\bar{p}_\perp} \simeq \frac{\bar{p}_\perp}{\Theta}\sqrt{1+\frac{\bar{p}_\perp^2}{2}} \exp\left(-\frac{\bar{p}_\perp^2}{2\Theta}\right) \tag{D6}$$

$$\simeq \frac{\bar{p}_\perp}{\Theta} \exp\left(-\frac{\bar{p}_\perp^2}{2\Theta}\right). \tag{D7}$$

The most likely $\bar{p}_\perp$ value given this probability distribution function is

$$\bar{p}_{\perp,\mathrm{ML}} = \sqrt{\Theta}. \tag{D8}$$

Data Availability Statement

The associated scripts that generate data and plots for this paper are available online (https://doi.org/10.22002/D1.1333).

Acknowledgments
The authors thank Mackenzie Wooten for reproducing some of the initial algebra. This material is based upon work supported by the Air Force Office of Scientific Research under award FA9550-17-1-0023 and by the National Science Foundation (NSF) Division of Atmospheric and Geospace Sciences under award 1914599.

References

Akalin, F., Gurnett, D. A., Averkamp, T. F., Persoon, A. M., Santolik, O., Kurth, W. S., & Hospodarsky, G. B. (2006). First whistler observed in the magnetosphere of Saturn. *Geophysical Research Letters*, *33*, L20107. https://doi.org/10.1029/2006GL027019

Albert, J. M. (2005). Evaluation of quasi-linear diffusion coefficients for whistler mode waves in a plasma with arbitrary density ratio. *Journal of Geophysical Research*, *110*, A03218. https://doi.org/10.1029/2004JA010844

Anderson, K. A., & Milton, D. W. (1964). Balloon observations of X rays in the auroral zone: 3. High time resolution studies. *Journal of Geophysical Research*, *69*(21), 4457–4479. https://doi.org/10.1029/JZ069i021p04457

Artemyev, A., Agapitov, O., Mourenas, D., Krasnoselskikh, V., Shastun, V., & Mozer, F. (2016). Oblique whistler-mode waves in the Earth's inner magnetosphere: Energy distribution, origins, and role in radiation belt dynamics. *Space Science Reviews*, *200*(1-4), 261–355. https://doi.org/10.1007/s11214-016-0252-5

Artemyev, A. V., Vasiliev, A. A., Mourenas, D., Agapitov, O. V., & Krasnoselskikh, V. V. (2013). Nonlinear electron acceleration by oblique whistler waves: Landau resonance vs. cyclotron resonance. *Physics of Plasmas*, *20*(12), 122901. https://doi.org/10.1063/1.4836595

Barbosa, D. D., & Kurth, W. S. (1993). On the generation of plasma waves in Saturn's inner magnetosphere. *Journal of Geophysical Research*, *98*(A6), 9351. https://doi.org/10.1029/93JA00477

Bellan, P. M. (2013). Pitch angle scattering of an energetic magnetized particle by a circularly polarized electromagnetic wave. *Physics of Plasmas*, *20*(4), 42117. https://doi.org/10.1063/1.4801055

Bellan, P. M. (2014). Fast, purely growing collisionless reconnection as an eigenfunction problem related to but not involving linear whistler waves. *Physics of Plasmas*, *21*(10), 102108. https://doi.org/10.1063/1.4897375

Bortnik, J., Thorne, R. M., & Inan, U. S. (2008). Nonlinear interaction of energetic electrons with large amplitude chorus. *Geophysical Research Letters*, *35*, L21102. https://doi.org/10.1029/2008GL035500

Boswell, R. W. (1984). Very efficient plasma generation by whistler waves near the lower hybrid frequency. *Plasma Physics and Controlled Fusion*, *26*(10), 1147–1162. https://doi.org/10.1088/0741-3335/26/10/001

Bourdier, A., & Gond, S. (2000). Dynamics of a charged particle in a circularly polarized traveling electromagnetic wave. *Physical Review E - Statistical Physics, Plasmas, Fluids, and Related Interdisciplinary Topics*, *62*(3 B), 4189–4206. https://doi.org/10.1103/PhysRevE.62.4189

Breneman, A. W., Crew, A., Sample, J., Klumpar, D., Johnson, A., Agapitov, O., et al. (2017). Observations directly linking relativistic electron microbursts to whistler mode chorus: Van Allen probes and FIREBIRD II. *Geophysical Research Letters*, *44*, 11,265–11,272. https://doi.org/10.1002/2017GL075001

Burtis, W. J., & Helliwell, R. A. (1969). Banded chorus—A new type of VLF radiation observed in the magnetosphere by OGO 1 and OGO 3. *Journal of Geophysical Research*, *74*, 3002–3010. https://doi.org/10.1029/JA074i011p03002

Cattell, C., Wygant, J. R., Goetz, K., Kersten, K., Kellogg, P. J., von Rosenvinge, T., et al. (2008). Discovery of very large amplitude whistler-mode waves in earth's radiation belts. *Geophysical Research Letters*, *35*, L01105. https://doi.org/10.1029/2007GL032009

Chai, K.-B., Zhai, X., & Bellan, P. M. (2016). Extreme ultra-violet burst, particle heating, and whistler wave emission in fast magnetic reconnection induced by kink-driven Rayleigh-Taylor instability. *Physics of Plasmas*, *23*(3), 32122. https://doi.org/10.1063/1.4944390

Chen, F. F., & Boswell, R. W. (1997). Helicons-the past decade. *IEEE Transactions on Plasma Science*, *25*(6), 1245–1257. https://doi.org/10.1109/27.650899

Coroniti, F. V., Kennel, C. F., Scarf, F. L., & Smith, E. J. (1982). Whistler mode turbulence in the disturbed solar wind. *Journal of Geophysical Research*, *87*(A8), 6029–6044. https://doi.org/10.1029/JA087iA08p06029

Gao, X., Li, W., Thorne, R. M., Bortnik, J., Angelopoulos, V., Lu, Q., et al. (2014). Statistical results describing the bandwidth and coherence coefficient of whistler mode waves using THEMIS waveform data. *Journal of Geophysical Research: Space Physics*, *119*, 8992–9003. https://doi.org/10.1002/2014JA020158

Ginet, G. P., & Heinemann, M. A. (1990). Test particle acceleration by small amplitude electromagnetic waves in a uniform magnetic field. *Physics of Fluids B: Plasma Physics*, *2*(4), 700–714. https://doi.org/10.1063/1.859307

Greenberg, O. W. (2002). CPT violation implies violation of Lorentz invariance. *Physical Review Letters*, *89*(23), 231602. https://doi.org/10.1103/PhysRevLett.89.231602

Gurnett, D. A., & O'Brien, B. J. (1964). High-latitude geophysical studies with satellite Injun 3: 5. Very-low-frequency electromagnetic radiation. *Journal of Geophysical Research*, *69*(1), 65–89. https://doi.org/10.1029/JZ069i001p00065

Hairer, E., & Wanner, G. (1991). *Solving Ordinary Differential Equations II, Springer Series in Computational Mathematics* (Vol. 14). Berlin, Heidelberg: Springer Berlin Heidelberg. (No. January 1996). https://doi.org/10.1007/978-3-662-09947-6

Haw, M. A., Seo, B., & Bellan, P. M. (2019). Laboratory measurement of large-amplitude whistler pulses generated by fast magnetic reconnection. *Geophysical Research Letters*, *46*, 7105–7112. https://doi.org/10.1029/2019GL082621

Helliwell, R. A., & Crystal, T. L. (1973). A feedback model of cyclotron interaction between whistler-mode waves and energetic electrons in the magnetosphere. *Journal of Geophysical Research*, *78*(31), 7357–7371. https://doi.org/10.1029/JA078i031p07357

Horne, R. B., & Thorne, R. M. (2003). Relativistic electron acceleration and precipitation during resonant interactions with whistler-mode chorus. *Geophysical Research Letters*, *30*(10), 1527. https://doi.org/10.1029/2003GL016973

Hospodarsky, G. B., Averkamp, T. F., Kurth, W. S., Gurnett, D. A., Menietti, J. D., Santolik, O., & Dougherty, M. K. (2008). Observations of chorus at Saturn using the Cassini Radio and Plasma Wave Science instrument. *Journal of Geophysical Research*, *113*, A12206. https://doi.org/10.1029/2008JA013237

Jeffrey, A., & Zwillinger, D. (2015. *Table of integrals, series, and products*. New York: Academic Press.

Jüttner, F. (1911). Das Maxwellsche Gesetz der Geschwindigkeitsverteilung in der Relativtheorie. *Annalen der Physik*, *339*(5), 856–882. https://doi.org/10.1002/andp.19113390503

Kennel, C. F., & Petschek, H. E. (1966). Limit on stably trapped particle fluxes. *Journal of Geophysical Research*, *71*(1), 1–28. https://doi.org/10.1029/JZ071i001p00001

Lakhina, G. S., Tsurutani, B. T., Verkhoglyadova, O. P., & Pickett, J. S. (2010). Pitch angle transport of electrons due to cyclotron interactions with the coherent chorus subelements. *Journal of Geophysical Research*, *115*, A00F15. https://doi.org/10.1029/2009JA014885

Leubner, M. P. (1982). On Jupiter's whistler emission. *Journal of Geophysical Research*, *87*(A8), 6335. https://doi.org/10.1029/JA087iA08p06335

Li, W., Thorne, R. M., Nishimura, Y., Bortnik, J., Angelopoulos, V., McFadden, J. P., et al. (2010). THEMIS analysis of observed equatorial electron distributions responsible for the chorus excitation. *Journal of Geophysical Research*, *115*, A00F11. https://doi.org/10.1029/2009JA014845

Livadiotis, G. (2016). Modeling anisotropic Maxwell-Jüttner distributions: Derivation and properties. *Annales Geophysicae*, *34*(12), 1145–1158. https://doi.org/10.5194/angeo-34-1145-2016

Lyons, L. R. (1974). Pitch angle and energy diffusion coefficients from resonant interactions with ion–cyclotron and whistler waves. *Journal of Plasma Physics*, *12*(3), 417–432. https://doi.org/10.1017/S002237780002537X

Lyons, L. R., Thorne, R. M., & Kennel, C. F. (1971). Electron pitch-angle diffusion driven by oblique whistler-mode turbulence. *Journal of Plasma Physics*, *6*(3), 589–606. https://doi.org/10.1017/S0022377800006310

Macúšová, E., Santolík, O., Cornilleau-Wehrlin, N., & Yearby, K. H. (2015). Bandwidths and amplitudes of chorus-like banded emissions measured by the TC-1 Double Star spacecraft. *Journal of Geophysical Research: Space Physics*, *120*, 1057–1071. https://doi.org/10.1002/2014JA020440

Mandt, M. E., Denton, R. E., & Drake, J. F. (1994). Transition to whistler mediated magnetic reconnection. *Geophysical Research Letters*, *21*(1), 73–76. https://doi.org/10.1029/93GL03382

Nunn, D. (1974). A self-consistent theory of triggered VLF emissions. *Planetary and Space Science*, *22*(3), 349–378. https://doi.org/10.1016/0032-0633(74)90070-1

Omura, Y., Furuya, N., & Summers, D. (2007). Relativistic turning acceleration of resonant electrons by coherent whistler mode waves in a dipole magnetic field. *Journal of Geophysical Research*, *112*, A06236. https://doi.org/10.1029/2006JA012243

Omura, Y., Katoh, Y., & Summers, D. (2008). Theory and simulation of the generation of whistler-mode chorus. *Journal of Geophysical Research*, *113*, A04223. https://doi.org/10.1029/2007JA012622

Omura, Y., Nunn, D., Matsumoto, H., & Rycroft, M. J. (1991). A review of observational, theoretical and numerical studies of VLF triggered emissions. *Journal of Atmospheric and Terrestrial Physics*, *53*(5), 351–368. https://doi.org/10.1016/0021-9169(91)90031-2

Omura, Y., & Summers, D. (2006). Dynamics of high-energy electrons interacting with whistler mode chorus emissions in the magnetosphere. *Journal of Geophysical Research*, *111*, A09222. https://doi.org/10.1029/2006JA011600

Pierrard, V., & Lazar, M. (2010). Kappa distributions: Theory and applications in space plasmas. *Solar Physics*, *267*(1), 153–174. https://doi.org/10.1007/s11207-010-9640-2

Qian, B.-L. (2000). Relativistic motion of a charged particle in a superposition of circularly polarized plane electromagnetic waves and a uniform magnetic field. *Physics of Plasmas*, *7*(2), 537–543. https://doi.org/10.1063/1.873839

Roberts, C. S., & Buchsbaum, S. J. (1964). Motion of a charged particle in a constant magnetic field and a transverse electromagnetic wave propagating along the field. *Physical Review*, *135*(2A), A381–A389. https://doi.org/10.1103/PhysRev.135.A381

Russell, C. T., Holzer, R. E., & Smith, E. J. (1969). OGO 3 observations of ELF noise in the magnetosphere: 1. Spatial extent and frequency of occurrence. *Journal of Geophysical Research*, *74*(3), 755–777. https://doi.org/10.1029/JA074i003p00755

Santolík, O., Gurnett, D. A., Pickett, J. S., Chum, J., & Cornilleau-Wehrlin, N. (2009). Oblique propagation of whistler mode waves in the chorus source region. *Journal of Geophysical Research*, *114*, A00F03. https://doi.org/10.1029/2009JA014586

Sentman, D. D., & Goertz, C. K. (1978). Whistler mode noise in Jupiter's inner magnetosphere. *Journal of Geophysical Research*, *83*, 3151–3165. https://doi.org/10.1029/JA083iA07p03151

Sudan, R. N., & Ott, E. (1971). Theory of triggered VLF emissions. *Journal of Geophysical Research*, *76*(19), 4463–4476. https://doi.org/10.1029/JA076i019p04463

Summers, D., Thorne, R. M., & Xiao, F. (1998). Relativistic theory of wave-particle resonant diffusion with application to electron acceleration in the magnetosphere. *Journal of Geophysical Research*, *103*(A9), 20,487–20,500.

Treumann, R. A., & Baumjohann, W. (2016). Anisotropic Jüttner (relativistic Boltzmann) distribution. *Annales Geophysicae*, *34*(9), 737–738. https://doi.org/10.5194/angeo-34-737-2016

Tsurutani, B. T., Lakhina, G. S., & Verkhoglyadova, O. P. (2013). Energetic electron (> 10 keV) microburst precipitation, ~5–15 s X-ray pulsations, chorus, and wave-particle interactions: A review. *Journal of Geophysical Research: Space Physics*, *118*, 2296–2312. https://doi.org/10.1002/jgra.50264

Tsurutani, B. T., & Smith, E. J. (1974). Postmidnight chorus: A substorm phenomenon. *Journal of Geophysical Research*, *79*(1), 118–127.

Tsurutani, B. T., Southwood, D. J., Smith, E. J., & Balogh, A. (1993). A survey of low frequency waves at Jupiter: The Ulysses encounter. *Journal of Geophysical Research*, *98*(A12), 21,203–21,216. https://doi.org/10.1029/93JA02586

Tsurutani, B. T., Verkhoglyadova, O. P., Lakhina, G. S., & Yagitani, S. (2009). Properties of dayside outer zone chorus during HILDCAA events: Loss of energetic electrons. *Journal of Geophysical Research*, *114*, A03207. https://doi.org/10.1029/2008JA013353

Vocks, C., Salem, C., Lin, R. P., & Mann, G. (2005). Electron halo and Strahl formation in the solar wind by resonant interaction with whistler waves. *The Astrophysical Journal*, *627*(1), 540–549. https://doi.org/10.1086/430119

Watson, G. N. (1995). *A treatise on the theory of Bessel functions*. Cambridge, UK: Cambridge University Press.

Yoon, Y. D., & Bellan, P. M. (2017). A generalized two-fluid picture of non-driven collisionless reconnection and its relation to whistler waves. *Physics of Plasmas*, *24*(5), 052114. https://doi.org/10.1063/1.4982812

Yoon, Y. D., & Bellan, P. M. (2018). An intuitive two-fluid picture of spontaneous 2D collisionless magnetic reconnection and whistler wave generation. *Physics of Plasmas*, *25*(5), 55704. https://doi.org/10.1063/1.5016345